Icarus **158**, 389–400 (2002)
doi:10.1006/icar.2002.6885

Models for Polar Haze Formation in Jupiter's Stratosphere

A. James Friedson

Earth and Space Sciences Division, MS 169-237, Jet Propulsion Laboratory, California Institute of Technology, Pasadena, California 91109
E-mail: Andrew.J.Friedson@jpl.nasa.gov

and

Ah-San Wong[1] and Yuk L. Yung

Department of Geological and Planetary Sciences, MS 150-21, California Institute of Technology, Pasadena, California 91125

Received October 9, 2001; revised April 1, 2002

We present coupled chemical–microphysical models for the formation, growth, and physical properties of the jovian polar haze based on a gas-phase photochemical model for the auroral regions developed by A. S. Wong *et al.* (2000, *Astrophys. J.* 534, L215–217). In this model, auroral particle precipitation provides an important energy source for enhanced decomposition of methane and production of benzene and polycyclic aromatic hydrocarbons (PAHs). We find that at high altitude, A_4 (pyrene, a hydrocarbon consisting of four fused aromatic rings) should homogeneously nucleate to form tiny primary particles. At lower altitudes, A_3 (phenanthrene) and A_2 (naphthalene) heterogeneously nucleate on the A_4 nuclei. These particles subsequently grow by additional condensation of A_2 on the nucleated particles and by coagulation and eventually sediment out to the troposphere. We run different cases of the aerosol microphysical model for different assumptions regarding the fractal dimension of aggregate particles formed by the coagulation process. If coagulation is assumed to produce spherical particles (of dimensionality 3), then their mean radius at altitudes below the 20-mbar pressure level is computed to be approximately 0.1 μm. If coagulation produces fractal aggregates of dimension 2.1, then their equivalent mean radius below the 20-mbar level is much larger, of order 0.7 μm. Aggregates with fractal dimensions between 2.1 and 3 form with equivalent mean radii between 0.1 and 0.7 μm. In every case, mean particle radius is found to decrease with increasing altitude, as expected for a system approximately in sedimentation–coagulation equilibrium. The predicted range of altitudes where aerosol formation occurs and the mean size to which particles grow are found to be generally consistent with observations. However, our calculations cannot presently account for the large amount of total aerosol loading inferred by M. G. Tomasko *et al.* (1986, *Icarus* 65, 218–243). We suggest that the primarily neutral chemical pathway to heavy hydrocarbon and PAH formation proposed by Wong *et al.* (2000) may proceed too slowly to produce a sufficient amount of condensible material. Inclusion of ion and ion–neutral reactions in the chemical scheme could potentially lead to the prediction of higher PAH production rates, higher nucleation rates, and greater aerosol loading, producing better agreement with the observations.

Key Words: **Jupiter; atmosphere; photochemistry; aurorae.**

I. INTRODUCTION

Stratospheric aerosol in Jupiter's atmosphere is concentrated in the polar regions (Hord *et al.* 1979, West *et al.* 1992). The polar hazes extend in altitude from as deep as the 100-mbar pressure level (Banfield *et al.* 1998) to as high as the ∼0.5-mbar level (West 1988). Since the time that Voyager 1 observations first established that the haze was situated principally in the stratosphere (Hord *et al.* 1979), it has been the subject of a number of theoretical and observational investigations, yet its origin and composition remain undetermined. The primary reason is the complexity of polar haze chemistry, which is thought to involve coupling among hydrocarbon photochemistry, ion–neutral chemistry, auroral processes, and particle microphysics. Previous models have investigated various aspects of the gas chemistry and particle microphysics separately, but to date no models have looked quantitatively at the coupled problem. The purpose of the present paper is to present results obtained from a coupled, one-dimensional photochemical–aerosol microphysical model designed to examine the question of polar haze formation with the intention of producing quantitative predictions of polar haze properties that can be compared with observations.

Two schemes dominated early discussions about the origin and composition of the polar aerosol. Strobel (1983) suggested that ammonia photolysis in the lower stratosphere leads to the production and condensation of hydrazine (N_2H_4); Hord *et al.* (1979) favored a model where auroral energetic breakdown of methane induces enhanced production of complex hydrocarbons, leading ultimately to the formation and growth of carbonaceous particles. The subsequent detection of certain complex hydrocarbons, most notably benzene, in the north polar region

[1] Present address: Department of Atmospheric, Oceanic, and Space Sciences, University of Michigan, Ann Arbor, MI 48109.

0019-1035/02 $35.00

(Kim *et al.* 1985) supports the latter view. Pryor and Hord (1991) found a geographical correlation between the auroral zones and UV-dark haze in the polar regions, providing additional evidence that haze production is linked to auroral energy deposition. This result has been confirmed by Vincent *et al.* (2000), who also observed transient aerosol features aligned with the auroral oval. Pryor and Hord (1991) proposed a sequence of ion–neutral reactions leading to the formation of heavy hydrocarbon ions that might serve as the precursors to carbonaceous aerosols. Unfortunately, they could not examine the implications of their chemical model in detail since the recombination products of the heavy hydrocarbon ions were unknown.

Recently, Wong *et al.* (2000, hereafter denoted W00) presented the results of a simple model for hydrocarbon photochemistry in the jovian aurorae. In their model, auroral particle precipitation provides an important energy source for enhanced decomposition of methane and production of benzene and heavier ring compounds. The maximum volume mixing ratio of benzene produced compares favorably with the observed value of $2^{+2}_{-1} \times 10^{-9}$ observed in the north polar region (Kim *et al.* 1985). Two-, three-, and four-hexagonal ring polycyclic aromatic hydrocarbons (PAHs) are predicted to be made in sufficient quantities to condense and form the haze. Accelerated decomposition of methane in the auroral zones is a crucial feature of the model, since it is essential for enhancing formation of benzene and heavier PAH species in the polar regions. Hence, if PAH chemistry is indeed a prologue to polar haze formation, we have a ready explanation for why the stratospheric hazes are concentrated near the poles and show geographic correlations with the auroral zones.

The work of W00 is important in that it represents the first attempt to quantitatively simulate the production of PAHs in Jupiter's polar stratosphere. PAHs are important molecular precursors of carbonaceous soot particle nucleation in laboratory combustion experiments (Richter and Howard 2000), and consequently it is plausible to think that they may also be important precursors for jovian polar haze formation. To examine this question further, we have developed a one-dimensional, coupled photochemical–aerosol microphysical model to simulate the hydrocarbon chemistry and aerosol processes simultaneously. Our principal goal is to determine what implications the chemical model has for haze particle size and aerosol loading and to compare these predictions with the available observations.

Our basic results can be summarized as follows. At high altitude, A_4 (pyrene, a hydrocarbon consisting of four fused hexagonal rings; hereafter we use the notation A_n to denote a PAH containing n fused hexagonal rings) homogeneously nucleates to form tiny primary particles. At lower altitudes, A_3 (phenanthrene) and A_2 (naphthalene) heterogeneously nucleate on the A_4 nuclei. These particles grow by additional condensation of A_2 on the nucleated particles and by coagulation and eventually sediment out to the troposphere. The predicted range of altitudes where aerosol formation occurs and the mean size to which particles grow are found to be generally consistent with the data analyses of Tomasko *et al.* (1986), West (1988), Rages *et al.* (1999), and Banfield *et al.* (1998). However, the model produces significantly less aerosol loading than that derived by Tomasko *et al.* (1986), suggesting that the total gas-to-particle conversion rate predicted by our model is too small.

In the following section, we discuss details of the coupled chemical–microphysical model. In Section III, we discuss the results of our simulations. These are compared to available observations in Section IV. We summarize our principal conclusions in Section V.

II. POLAR HAZE MODEL

To simulate the physical properties and spatial distribution of aerosols forming in the jovian auroral regions, our model couples the chemical model of W00 with an aerosol microphysical model, some aspects of which have been described previously (Friedson 1998). A schematic diagram of the basic physical processes included in the model is shown in Fig. 1. The one-dimensional chemical model calculates the steady-state vertical profiles of hydrocarbon species that emerge as a result of decomposition of CH_4 due to photolysis and auroral particle precipitation. A series of effectively irreversible reactions leads

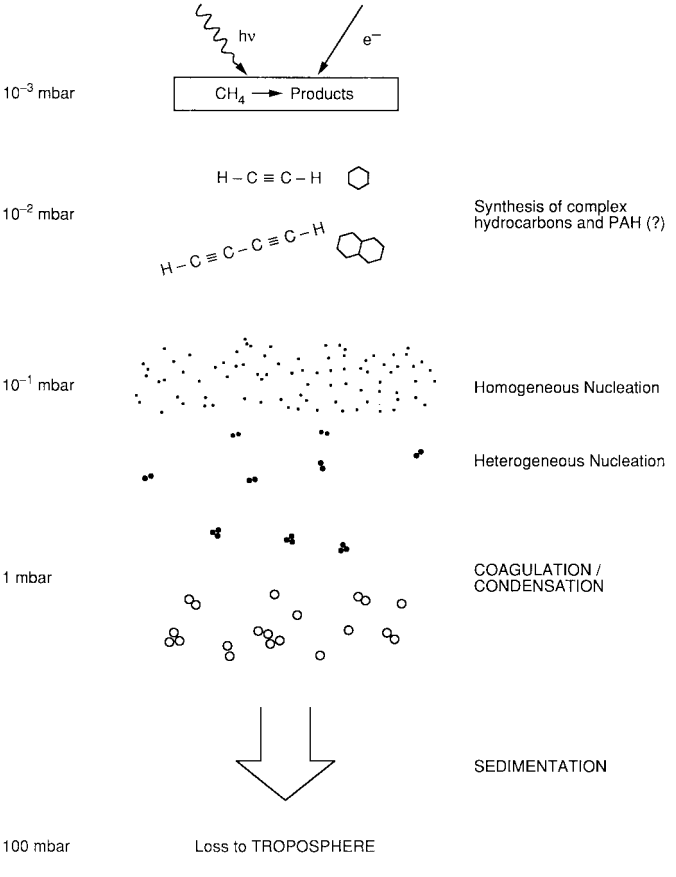

FIG. 1. Schematic diagram of physical processes included in the coupled chemical–aerosol microphysical model.

to the production of stable PAH species which become highly saturated below the ∼0.15-mbar pressure level. Homogeneous nucleation of the least volatile of the saturated species forms tiny nuclei, upon which other saturated species may heterogeneously nucleate. Both the pure and mixed particles subsequently grow by condensation of any remaining vapor and by coagulation. As particles grow, they sediment under the effect of gravity until they reach the troposphere, where they lose their identity as stratospheric aerosols upon mixing with tropospheric cloud particles. The aerosol loading of the polar stratosphere reaches a steady state when the column-integrated mass production rate of condensed material due to nucleation is balanced by the net mass flux into the troposphere due to sedimentation and eddy mixing. Transport of aerosol away from the auroral source regions by horizontal winds is not included in this one-dimensional model. By ignoring this transport, the one-dimensional model will tend to overestimate aerosol column abundances. More complex simulations that include horizontal transport should be carried out once measurements of high-altitude winds in Jupiter's polar stratosphere become available.

The altitude range of the calculations extends from the 100-mbar level up to the 0.1-μbar level, using five grid points per pressure scale height. Temperatures in the auroral regions are considerably warmer than that in nonauroral regions due to the excess heating generated by precipitating particles (Grodent *et al.* 2001). For a nominal auroral region temperature profile, we used one recommended by Trafton *et al.* (1994), shown as the solid curve in Fig. 2. This profile, which was also used by W00,

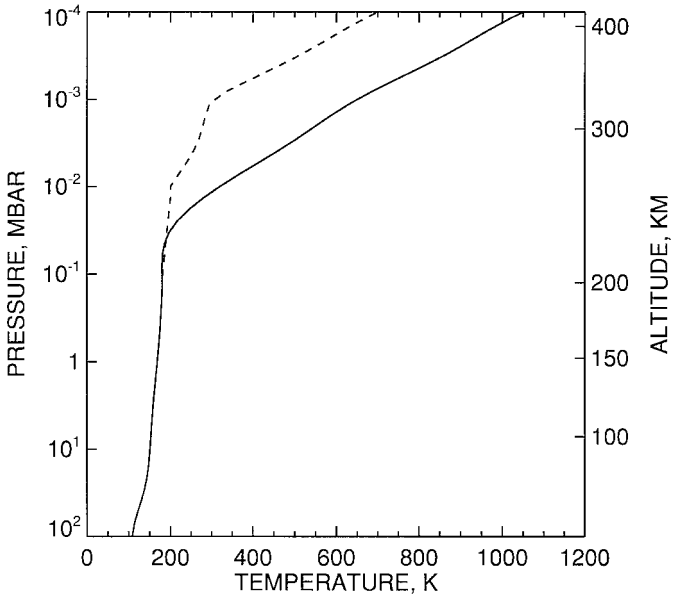

FIG. 2. Auroral region temperature profiles used in the model. The solid curve is nominal profile, recommended by Trafton *et al.* (1994). The dashed curve is a colder profile based on the "diffuse auroral" model of Grodent *et al.* (2001). The altitude scale on the right refers to height above the 1-bar pressure level in the nonauroral atmosphere as determined by the Galileo Atmospheric Structure Instrument (Seiff *et al.* 1998).

is somewhat warmer than the warmest profile ("discrete auroral case") calculated by Grodent *et al.* (2001) in their self-consistent model of the jovian auroral thermal structure. As shown by Grodent *et al.*, significantly colder thermal profiles are also consistent with existing observational constraints. Consequently, to test the sensitivity of the results to temperature, we reran some of the simulations using a much colder temperature profile based on the "diffuse auroral" thermal profile of Grodent *et al.* (2001). This colder profile is shown as the dashed curve in Fig. 2.

Chemical Model

We calculate the effects of gas-phase chemistry in the auroral regions using the chemical model of W00. This kinetic model includes 314 neutral gas-phase chemical and photolytic reactions involving hydrocarbon species up to pyrene (A_4). It also includes seven reactions involving dissociative recombination of CH_5^+ and H_3^+ ions. The rates for the recombination reactions are based on the auroral model of Perry *et al.* (1999). Perry *et al.* carried out electron transport calculations to model the effects of a monoenergetic spectrum of precipitating electrons with energies ranging between 20 and 100 keV and presented the dissociation and ionization rates of various ionic species for each assumed energy. W00 adopted recombination rates corresponding to an assumed precipitating flux of 11 erg cm^{-2} s^{-1} of 30-keV electrons and found that this auroral energy input enhanced the destruction rate of methane by a factor of ∼25 over that of photolysis at 60°. Far-UV emission rates deduced from auroral spectra and images indicate that the average energy flux of ∼30-keV electrons may in fact be higher than ∼100 erg cm^{-2} s^{-1} (Grodent *et al.* 2001), about a factor of 10 higher than assumed by W00. Hence, W00 may have underestimated the destruction rate of methane in the auroral regions by a significant factor. The reaction scheme and rates for light hydrocarbons and heavier aliphatic species are based on the work of Gladstone *et al.* (1996), with updates described by Lee *et al.* (2000). The reaction scheme and rates for PAH species are derived largely from laboratory and modeling studies of soot formation during fuel-rich hydrocarbon combustion (e.g., Wang and Frenklach 1994). There is a paucity of experimental data for the cyclization reactions beyond the first aromatic ring (benzene). In the absence of measurements, kinetic rates for these reactions are estimated using the concept of reaction classes, where reactions are grouped according to their similarity to a prototype reaction whose rate has been measured or is usefully constrained. The rate coefficient expression for the prototype reaction is then assigned to all reactions grouped in the same class (Frenklach *et al.* 1985). It should be kept in mind, however, that the kinetics of PAH formation is still an active area of investigation in the combustion research community, with rate constants being revised and updated continually. Moreover, many of the rate constants used here have been measured or estimated only for higher temperatures than pertain to the lowest altitudes in our model; extrapolation of these rates to lower temperatures is therefore required. In addition, many possible ion–neutral reactions that may

be important are ignored in this preliminary study. While some measure of comfort is gained by the fact that the model of W00 produces a maximum benzene volume mixing ratio in rough agreement with the observed value, it is clear that these calculations will probably require revision in the future as additional experimental data become available.

Aerosol Microphysical Model

We use an aerosol microphysical model (AMM) to simulate the nucleation, growth, and sedimentation of the polar haze particles, based on numerical algorithms developed by O. B. Toon, R. C. Turco, and colleagues. Toon *et al.* (1988) describe in detail the numerical implementation of the algorithms we use for vertical transport (including sedimentation), coagulation, and condensation/evaporation; we have used these algorithms without modification. In the following we discuss our treatment of particle nucleation, as well as certain modifications made to the coagulation kernel and sedimentation rates to account for the fact that the polar haze particles most likely consist of amorphous aggregates of primary particles.

The less massive, more volatile hydrocarbons do not condense in Jupiter's stratosphere. Kim *et al.* (1995) suggested that benzene might condense below the 20-mbar level and be the chief ingredient of the polar haze. Benzene does not condense in the W00 model, however; its mixing ratio falls sharply with decreasing altitude below its peak near the 0.1-mbar level and it remains undersaturated above the 100-mbar level despite the cold temperatures of the lower stratosphere. The heavier stable PAHs A_2, A_3, and A_4 are less volatile than benzene and are predicted to become supersaturated, below the $\sim$0.03-mbar level for A_3 and A_4 and below the $\sim$0.3-mbar level for A_2. For condensation of these species to proceed, however, they must first homogeneously or heterogeneously nucleate to form tiny condensation nuclei held together by weak van der Waals forces.

Homogeneous and heterogeneous nucleation (on water surface) of A_2 has been studied in the laboratory by Smolik *et al.* (1986), Smolik and Zdimal (1993), and Smolik and Schwartz (1997). The experiments consisted of determining the critical saturation ratio of vapor required to yield a prescribed nucleation rate (taken to be $\sim$5 particles cm^{-3} s^{-1} in the homogeneous nucleation experiments and $\sim$100 nuclei cm^{-2} s^{-1} in the heterogeneous nucleation experiment) over a range of temperatures. In general, Smolik and co-workers found that classical nucleation theory provides an adequate approximation for the critical saturation ratio for both types of nucleation. The experiments were conducted at temperatures significantly higher than those where A_2 is supersaturated in Jupiter's stratosphere. (A_2 in the chemical model of W00 saturates below the $\sim$0.3-mbar level, where stratospheric temperatures are below 180 K, while the lowest experimental temperature was 228 K). Extrapolation of the classical homogeneous nucleation rate inferred from the critical saturation ratio data to low temperatures indicates that the homogeneous nucleation of A_2 is unlikely to be important in Jupiter's stratosphere, since the maximum homogeneous nucleation rate above the 100-mbar level is found to be much less than 10^{-10} cm^{-3} s^{-1}. The primary reason for this low nucleation rate can be found in the high surface tension of solid A_2 combined with the fact that only moderately high saturation ratios are attained by A_2 in the stratosphere.

For comparison, one can estimate the order of magnitude of the minimum nucleation rate necessary to explain the observations: The column abundance N of aerosol in the polar regions is of order $N \sim 10^8$ cm^{-2} (Tomasko *et al.* 1986) and the residence time of the aerosol is at most of order $\tau \sim 10^9$ s (the eddy diffusion timescale at the 100 mbar level); hence the minimum column-integrated nucleation rate above the 100-mbar level must be $N/\tau \sim 0.1$ cm^{-2} s^{-1}. This corresponds to a lower limit since condensation and coagulation can only decrease the total number of particles in the population. The implied minimum nucleation rate averaged over a column of depth $\sim 10^7$ cm (about 3 pressure scale heights) is $J_{\min} \sim 10^{-8}$ cm^{-3} s^{-1}, which is about 100 times larger than the upper bound on the A_2 homogeneous nucleation rate given in the previous paragraph. It must be noted, however, that classical nucleation theory can grossly underestimate the nucleation rate at low temperatures, where the critical nucleus may consist of only a few molecules (Keesee 1989). It is therefore possible that homogeneous nucleation of A_2 contributes to particle formation in the coldest layers of Jupiter's stratosphere, but in general we expect heterogeneous nucleation of A_2 on preexisting grains of mixed A_3–A_4 composition to dominate.

Much of the critical data necessary to calculate the homogeneous nucleation rate of A_3 and A_4 are unavailable. However, these species develop very high saturation ratios in those layers where their production rates are high and their equilibrium vapor pressures are very low. The saturation ratio of A_4 reaches $\sim 10^7$ near the 0.2-mbar level and increases rapidly with decreasing altitude. For these high saturation ratios, the critical cluster size for homogeneous nucleation predicted by classical theory becomes less than one molecule. The situation is analogous to the high saturation ratio conditions occurring in experiments on refractory particle synthesis in laboratory flames (Ulrich 1971, Zachariah and Semerjian 1989). Under such conditions, nucleation is seen to immediately follow chemical production of the precursor species, producing a large number of tiny primary particles. Almost all the vapor is depleted in forming these particles. Growth proceeds by Brownian coagulation of the primary particles. When the initial chemical reaction and nucleation times are short compared to the total coagulational growth period, the growth is controlled by the frequency of Brownian collisions between primary particles and is effectively independent of the early history of the system. Under these conditions, the effective size of the resulting agglomerates can be accurately predicted using a simple model of coagulating monomers. In our model, we take the homogeneous nucleation rate of the very highly saturated species to equal their bimolecular collision rate. The dimers thus formed are then allowed to coagulate via Brownian motion

to form larger clusters. These subsequently serve as effectively involatile condensation nuclei, upon which A_2 and A_3 heterogeneously nucleate and condense.

Heterogeneous nucleation of condensible vapor on preexisting grains is generally far more efficient than homogeneous nucleation of the vapor. Again, data on interfacial surface tensions for the A_2–A_3–A_4 system are unavailable for calculating the classical heterogeneous nucleation rate of A_2 and A_3 on A_4 surfaces. To make progress, we follow Turco *et al.* (1982) and consider only the maximum possible value for the nucleation rate per condensation nucleus, which occurs when there is effectively no energy barrier to nucleation. In this formulation, A_4 (or mixed A_3–A_4) particles which are supersaturated with respect to the A_2 or A_3 vapor are assumed to become activated in the time required to deposit a monolayer of condensate over the surface of the particle. There is in fact some experimental evidence that this very simple treatment may, in some instances, yield better results than the classical theory, even when the surface interface properties of the materials are well known (Chen *et al.* 1993). The timescale for heterogeneous nucleation is given by

$$\tau_{\rm het}^{-1} = \pi \left(\frac{3\mu_{A_i}}{4\pi\rho_{A_i} N_{\rm A}} \right)^{2/3} v_{A_i} c_i, \tag{1}$$

where μ_{A_i} is the molecular weight of A_i, ρ_{A_i} is the density of the solid, $N_{\rm A}$ is Avogadro's number, v_{A_i} is the thermal velocity of the vapor, c_i is its concentration, and i equals 2 or 3. Notice that $\tau_{\rm het}$ is independent of the size of the condensation nucleus.

The Brownian coagulation kernel and sedimentation velocity of aerosol particles are sensitive to their geometric shape. Coagulation of clusters of relatively involatile material tends to form amorphous aggregates possessing a characteristic fractal dimensionality (Mountain *et al.* 1986, Meakin and Jullien 1988). Computer models of the cluster aggregation process tend to yield structures with fractal dimensions ranging from $D \simeq 1.8$ for diffusion-limited aggregation to $D \simeq 1.95$ for ballistic aggregation. (Ballistic aggregation occurs in the "free-molecular" regime; also note that $D = 3$ corresponds to nonfractal solid shapes such as spheres, cubes, etc.) Including the effects of restructuring of aggregates during the collision process in computer models increases characteristic fractal dimensions to $D \simeq 2.1$ (Meakin and Jullien 1988). Examples of fractal aggregates simulated by computer models can be found in Meakin and Jullien (1988) and Meakin *et al.* (1989), while electron photomicrographs of aggregate particles found in nature can be found in Fuchs (1964, Fig. 8) and Chung *et al.* (1992). In nature, fractal aggregates typically form with somewhat higher dimensionality; for example, $D \simeq 2.6$ for fumed silica (Freltoft *et al.* 1986). Since observations of jovian polar haze particles suggest that they are amorphous aggregates of small monomers (West and Smith 1991), it is of interest to explore coagulation and sedimentation for particles with fractal dimensions $1.8 \leq D \leq 3$.

Coagulation rates tend to be faster for particles with $D < 3$. For agglomerates of fractal dimension D, the coagulation kernel can be written (Mountain *et al.* 1986)

$$K_{ij} = \left(\frac{4\pi}{3} \right)^{1/2} \alpha_{\rm s} d^2 B^2 \left[\frac{6kT}{\rho_0} \right]^{1/2} \left[\left(\frac{v_i}{v_1} \right)^{1/D} + \left(\frac{v_j}{v_1} \right)^{1/D} \right]^2 \times \left(\frac{1}{v_i} + \frac{1}{v_j} \right)^{1/2} \tag{2}$$

for the "free-molecular" regime, in which the ratio (Knudsen number) of the mean free path l to the effective radius of the particle (gyration radius $R_{\rm g}$) is ${\rm Kn} \equiv l/R_{\rm g} \gg 1$, and is

$$K_{ij} = \frac{2kT}{3\eta} \alpha_{\rm s} \left[\left(\frac{v_i}{v_1} \right)^{1/D} + \left(\frac{v_j}{v_1} \right)^{1/D} \right] \left(\left(\frac{v_1}{v_i} \right)^{1/D} + \left(\frac{v_1}{v_j} \right)^{1/D} \right) \tag{3}$$

for the "continuum" regime in which ${\rm Kn} \ll 1$. In these expressions, v_i is the volume of a cluster containing i primary particles, d is the diameter of the primary particles, B is a fit parameter ($B \simeq 0.4$), ρ_0 is the bulk condensate density, k is Boltzmann's constant, T is temperature, η is the dynamic viscosity of molecular hydrogen, and $\alpha_{\rm s}$ is a sticking probability, usually taken to be of order unity for neutral particles. The gyration radius $R_{\rm g}$ is related to the second moment of the mass distribution about the center of mass of the agglomerate (Mountain *et al.* 1986). The Brownian coagulation kernel for spherical particles is recovered from these expressions when $D = 3$ (Turco *et al.* 1982). In our code, we interpolate the coagulation kernel between the free-molecular and continuum regimes using a method given by Jacobson (1999) that is based on an earlier formulation provided by Fuchs (1964).

The terminal velocity of sedimentation $v_{\rm s}$ for an agglomerate of fractal dimension D is given by (Meakin *et al.* 1989)

$$v_{\rm s} = -\frac{Mg}{6\pi\eta R_{\rm g}} \left[1 + \frac{9}{2} \frac{\phi}{\delta} \frac{\pi R_{\rm g}^2}{\sigma(s) d^2} {\rm Kn}\, e^{-2/{\rm Kn}} \right], \tag{4}$$

where s is the number of primary particles in the aggregate, $R_{\rm g} = Bs^{1/D}d$ is the gyration radius, M is the total particle mass, g is the gravitational acceleration, $\sigma(s) = \beta_1 s^{\gamma_1} + \beta_2 s^{\gamma_2}$ gives the dependence of the effective collision cross section on s, $\phi = \eta/(nmvl)$, n is the local gas density, m is the mass of an H_2 molecule, v is the mean thermal velocity, and δ is a parameter that describes the molecular collision process involved in gas-particle momentum transfer (i.e., specular scattering or cosine-law diffuse scattering; Turco *et al.* 1982). Meakin *et al.* (1989) give values for β_1, β_2, γ_1, and γ_2 for various values of D. The expression for $v_{\rm s}$ has been written in such a way as to recover the high-Kn-number formula given by Turco *et al.* (1982) for spherical particles when $D = 3$. It also has the interesting property that, at high Kn, the sedimentation velocity

is approximately independent of the agglomerate's mass when $D < 2$ (Meakin *et al.* 1989).

III. RESULTS

In this section, we present the results of one-dimensional, coupled chemical–microphysical simulations of polar haze formation, growth, and vertical transport. The numerical experiments have been conducted assuming that coagulation produces either spherical particles or amorphous clusters characterized by a single fractal dimension.

The steady-state volume mixing ratios of the PAHs A_1, A_2, A_3, and A_4 produced by the model are plotted in Fig. 3, together with the saturation equilibrium mixing ratio corresponding to each species. The A_4 mixing ratio drops steeply below the 0.2-mbar pressure level where A_4 attains saturation ratios greater than $\sim 10^7$ and homogeneously nucleates. This nucleation reaches a maximum value of 2×10^{-3} cm^{-3} s^{-1} at the 0.2-mbar level and consumes nearly all of the A_4 vapor. Supersaturated A_3 heterogeneously nucleates on the A_4 condensation nuclei immediately after they are formed. The more volatile A_2 heterogeneously nucleates on the mixed A_3–A_4 particles below the ~0.3-mbar level. The mixing ratios of A_2, A_3, and A_4 vapor are lowered by condensation to less than 1 part per trillion at altitudes below the 2-mbar level. If condensation is not included, the chemical model predicts a 2-mbar level mixing ratio of ~0.2 parts per billion for all three PAHs.

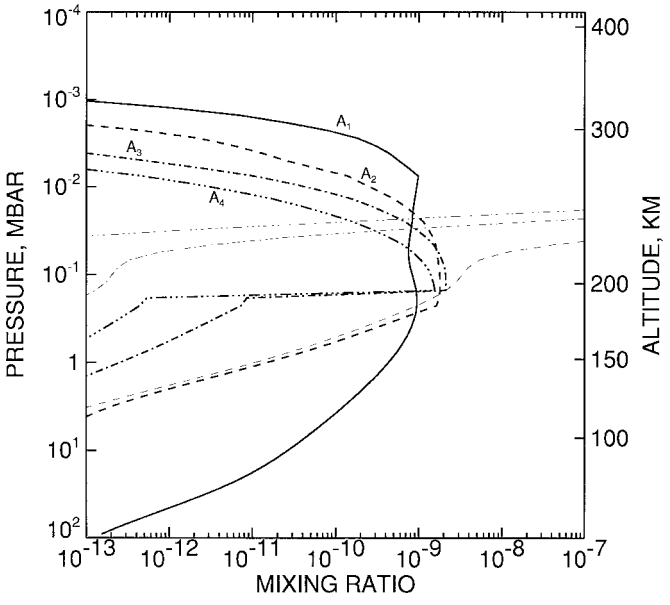

FIG. 3. Steady-state volume mixing ratios of PAHs in the auroral zones computed by the coupled chemical–microphysical model. A_1 (benzene) (solid); A_2 (naphthalene) (dashed); A_3 (phenanthrene) (dash-dot); A_4 (pyrene) (dash-dot-dot-dot). The thin lines indicate the saturated equilibrium mixing ratios of A_2 (dashed), A_3 (dash-dot), and A_4 (dash-dot-dot-dot) vapor. Sharp drops in the mixing ratios of A_2, A_3, and A_4 demarcate the onset of nucleation and condensation. The altitude scale is explained in the caption for Fig. 2.

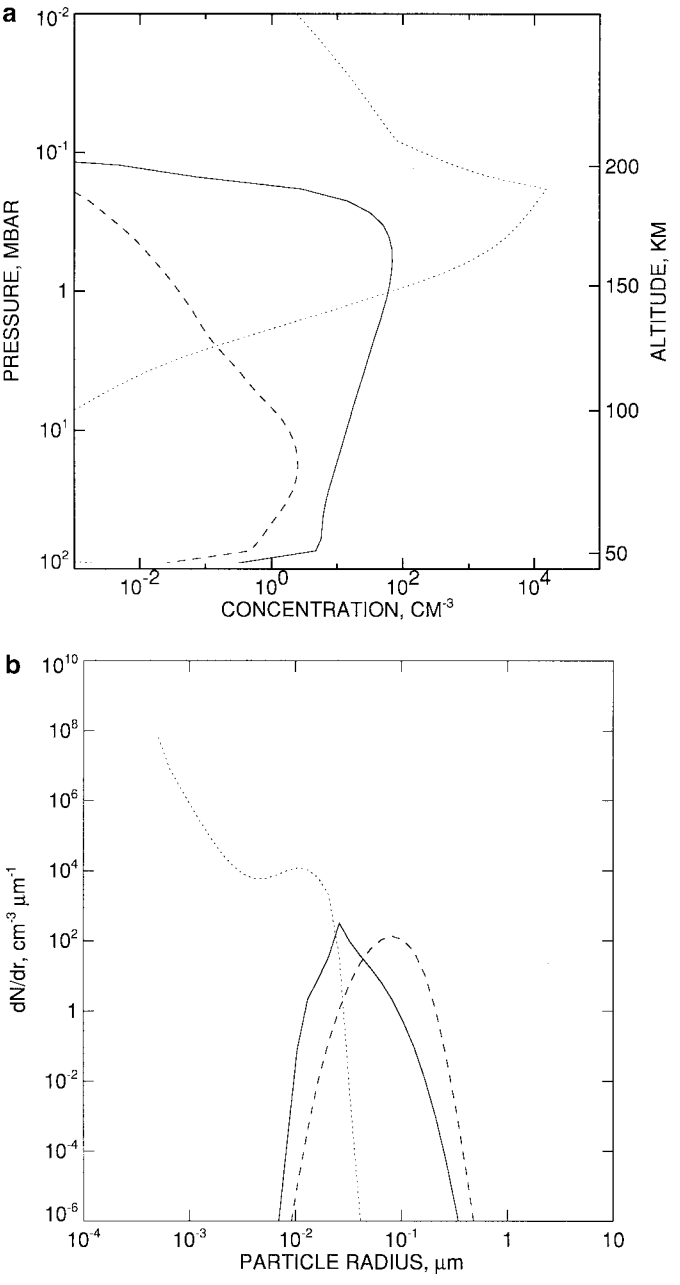

FIG. 4. Results for spherical particles. (a) The solid curve is the total concentration of mixed A_2–A_3–A_4 particles with radii greater than 0.01 μm vs pressure. The dashed curve is the concentration of particles with radii between 0.09 and 0.11 μm. The dotted curve is the total concentration of bare A_3–A_4 nuclei. The sharp decrease in concentrations near the 100-mbar level reflects a model-imposed dynamical removal of particles to the troposphere on a timescale of 9×10^5 s. (b) Size distributions of mixed A_2–A_3–A_4 particles at the 0.5-mbar (solid) and 20-mbar (dashed) pressure levels. The dotted curve shows the size distribution of bare A_3–A_4 nuclei at the 0.5-mbar level.

Figure 4a shows vertical profiles of the steady-state concentration of mixed A_2–A_3–A_4 particles, formed under the assumption that coagulation produces spherical aggregates with dimensionality $D = 3$. While we expect true agglomeration of refractory

PAHs to lead to clusters with fractal dimensions $D < 3$, $D = 3$ is useful to examine as a limiting case because it applies to aerosols with the most compact structure possible. The solid curve in Fig. 4a represents the vertical profile of total concentration of mixed A_2–A_3–A_4 particles with radii greater than 0.01 μm. The dashed curve represents the concentration of these particles having radii between 0.09 and 0.11 μm. Also shown in the figure is the total concentration of bare A_3–A_4 nuclei that do not nucleate A_2 on their surfaces. The total mixed particle concentration peaks near 1 mbar and is dominated by particles with radii less than $\sim$0.03 μm. The location of this peak coincides with the altitude where the sedimentation fall time for the small particles (defined as the time required for a particle to sediment one pressure scale height) becomes comparable to their coagulation removal timescale. Above the 1-mbar level, the fall time of tiny particles injected by A_4 nucleation is short compared to their coagulation removal timescale, and they quickly sediment to the 1-mbar level before appreciable coagulational growth can occur. As they fall, their terminal sedimentation velocity decreases with depth in response to the exponentially increasing aerodynamic drag of the background gas and their concentration increases in order to conserve the total flux. Below the 1-mbar level, the fall time of the particles exceeds the coagulation removal timescale and there is plenty of time for the small particles to coagulate to form larger, but fewer, particles. The same line of reasoning can be applied to particles in any given size range. We thus expect the peak in the vertical profile of any such population of particles to occur roughly at the altitude where their fall time and coagulation removal timescale become comparable. Since large particles fall faster than small ones at any given pressure level, their fall time becomes comparable to their coagulation removal timescale at lower altitudes, and thus the vertical profile for particles having radii between 0.09 and 0.11 μm shown in Fig. 4a peaks at a lower altitude than that for the cumulative population, which is dominated by smaller particles.

For the same reason, we expect the largest particles in the aerosol population to be concentrated toward the lowest altitudes. This is demonstrated in Fig. 4b, where we plot the steady-state size distributions of mixed A_2–A_3–A_4 particles at the 0.5-mbar level (solid curve) and 20-mbar level (dashed curve). Near the 0.5-mbar level, the mean particle radius is 0.03 μm, which is only slightly larger than the critical radius for heterogeneous nucleation of A_2 at this altitude. There also exists at this altitude a large population of bare A_3–A_4 nuclei (shown as the dotted curve) with radii less than $\sim$0.02 μm. Because of the Kelvin effect (e.g., Keesee 1989), in which the finite radius of curvature of the interface increases the vapor pressure in equilibrium with a spherical droplet relative to that of the bulk condensate, the saturation ratio of A_2 over these tiny particles remains below unity and they are prevented from inducing heterogeneous nucleation. At the 20-mbar level, the mean particle radius is found to be significantly larger, $\sim$0.08 μm. We can understand how this mean radius is selected by noting that it is approximately the radius of a particle for which the fall time at this altitude is comparable to the coagulation removal timescale. Simply put, particles smaller than $\sim$0.08 μm at the 20-mbar level grow by coagulation before settling out, while particles larger than this mean radius fall out before they grow any further by coagulation. Condensation of A_2 vapor onto heterogeneously nucleated A_3–A_4 grains also contributes to the growth of particles below the $\sim$0.5-mbar level but makes a smaller contribution than coagulation. The reason for this can be traced to the very low absolute concentrations of A_2 in the jovian stratosphere.

Quite different results for polar haze vertical distribution and mean particle radius are obtained when we assume that coagulation produces fractal aggregates rather than spherical particles. The difference stems primarily from the much longer sedimentation fall times associated with fractal aggregates. Figure 5a displays fall time vs pressure for spherical particles of radius 0.05 μm and 0.5 μm. At the 0.5-mbar pressure level, the time for a 0.5-μm radius spherical particle to fall one scale height is $\sim 2 \times 10^5$ s; that for a 0.05-μm particle is $\sim 2 \times 10^6$ s. In Fig. 5b, we show fall time vs pressure for aggregate particles with fractal dimension $D = 2.10$, as might be formed by ballistic aggregation with restructuring (Meakin and Jullien 1988). The fall time for a 0.5-μm radius aggregate (for aggregates, we use the word "radius" to refer to the radius of a spherical particle that would have the same volume as the aggregate; note that this is generally smaller than the gyration radius of the aggregate) at the 0.5-mbar level is now $\sim 10^7$ s, or $\sim$50 times longer than the fall time of a spherical particle of the same mass. Similarly, the fall time for a 0.05-μm radius aggregate is $\sim$20 times longer than that of a spherical particle of the same mass. Hence, aggregates with $D = 2.10$ fall much more slowly in Jupiter's lower stratosphere than spherical particles. This is because they encounter a greater aerodynamic drag force than do their spherical equivalents as a result of their larger projected cross section. At low altitudes in Jupiter's stratosphere, the fall times of small aggregate particles can exceed the eddy diffusion timescale. For these particles, eddy diffusion rather than sedimentation becomes the primary mechanism for vertical transport.

Since fractal aggregate particles have longer residence times in the stratosphere than their spherical counterparts, they have more time to coagulate and form larger clusters. Figure 6 shows the results for aggregates with fractal dimension $D = 2.10$. In Fig. 6a, the total concentration of mixed A_2–A_3–A_4 particles with equivalent radii greater than 0.01 μm is plotted against pressure. Also shown is the concentration of particles having radii between 0.73 and 0.92 μm. The total concentration peaks near the 1-mbar level for essentially the same reason as in the spherical cluster case; the sedimentation fall time and coagulation removal timescale are about equal at this altitude for the average particle. However, the total aerosol population now consists of fewer, but larger, particles. This can be seen in Fig. 6b, where the size distributions of fractal aggregates with $D = 2.10$ are plotted for the 0.5-mbar and 20-mbar pressure levels. The mean particle radius is now found to be 0.3 μm at the 0.5-mbar level and 0.7 μm at the 20-mbar level. These mean radii are a

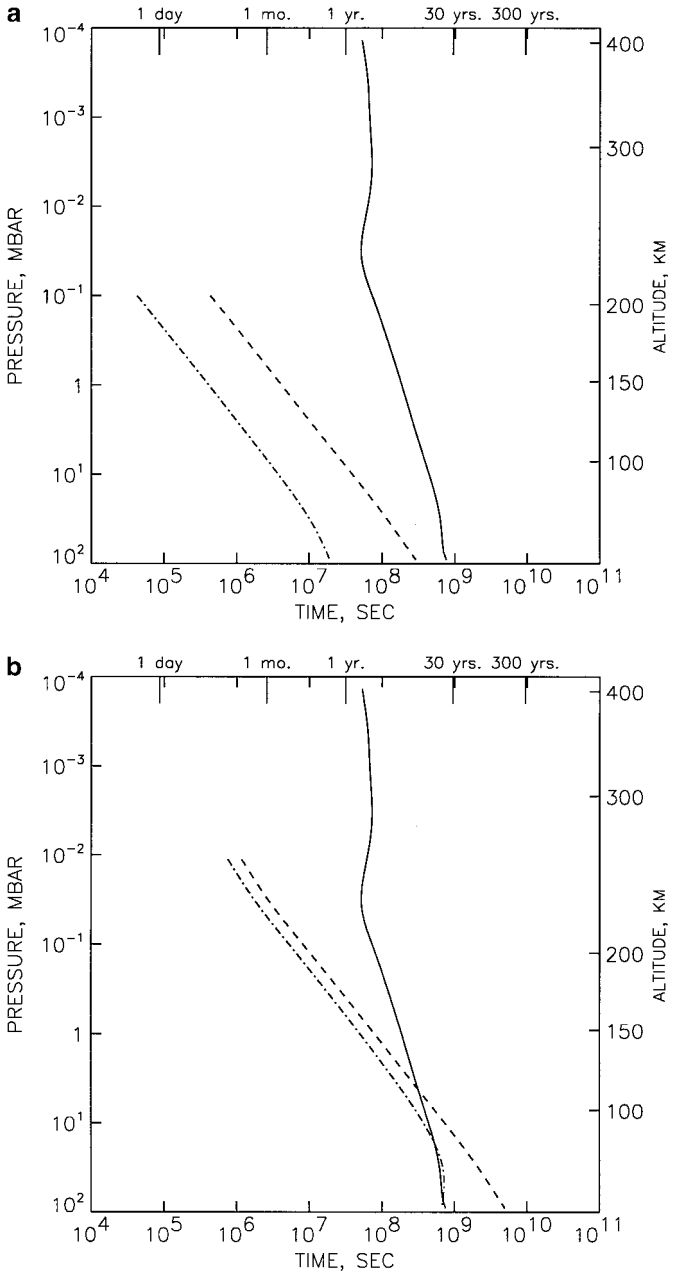

FIG. 5. (a) Fall times for spherical particles of radius 0.05 μm (dashed) and 0.5 μm (dash-dot). The thin solid line indicates the eddy diffusion timescale. (b) Fall times for aggregate particles with fractal dimension $D = 2.1$. Fall times are shown for aggregates with spherical-equivalent radii of 0.05 μm (dashed) and 0.5 μm (dash-dot). The aggregates fall slower than spherical particles of the same mass because they encounter a greater aerodynamic drag force due to their larger projected cross section.

factor ~10 greater than those predicted for spherical particles at the same altitudes. The mean radius of the aggregates decreases monotonically with altitude; this is also true for the spherical particle case.

We also ran our microphysical model for aggregates with fractal dimension $D = 1.8$, the smallest fractal dimension obtained in computer simulations of the aggregation process. Aggregates in nature generally form with significantly higher D (Meakin and Jullien 1988). Hence, $D = 1.8$ roughly corresponds to the fractal dimension of the most loosely knit aggregates that can be formed by coagulation. The results for $D = 1.8$ are found to differ very

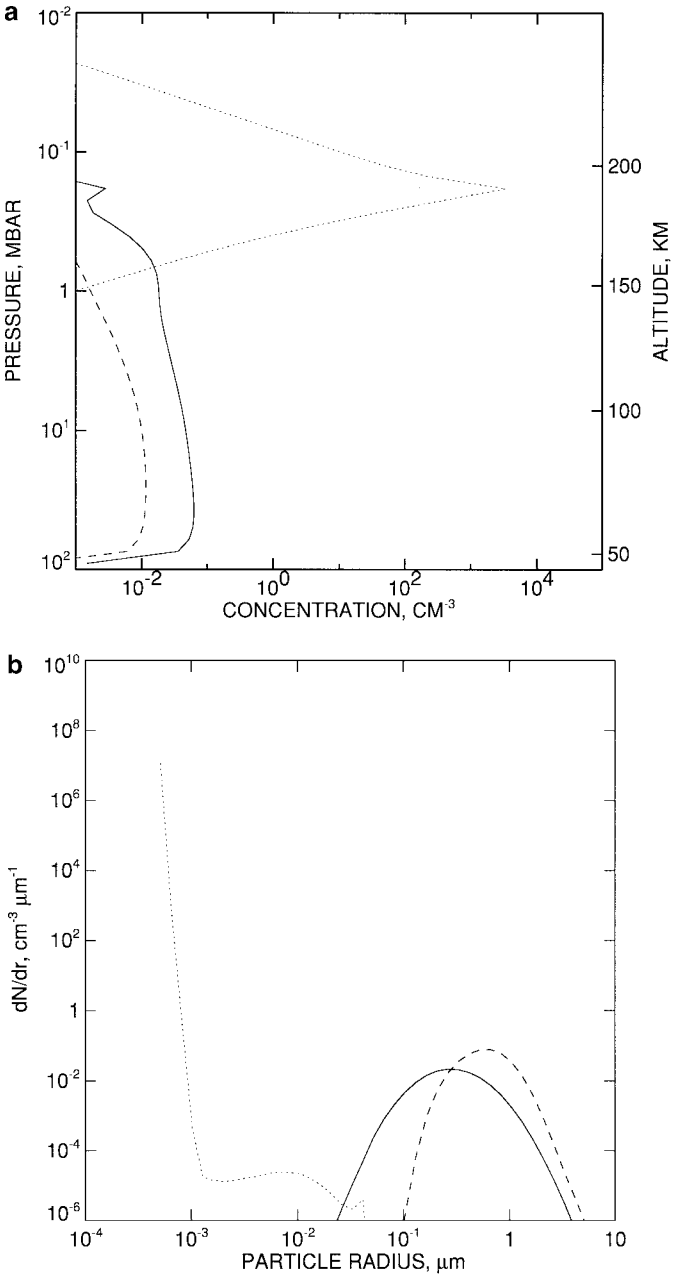

FIG. 6. Results for aggregates with fractal dimension $D = 2.1$. (a) The solid curve is the total concentration of mixed A_2–A_3–A_4 particles with equivalent radii greater than 0.01 μm vs pressure. The dashed curve is the concentration of particles with radii between 0.73 and 0.92 μm. The dotted curve is the total concentration of bare A_3–A_4 nuclei. (b) Size distributions of mixed A_2–A_3–A_4 particles at the 0.5-mbar (solid) and 20-mbar (dashed) pressure levels. The dotted curve shows the size distribution of bare A_3–A_4 nuclei at the 0.5-mbar level.

little from those presented for $D = 2.10$. We therefore expect the results shown for $D = 2.10$ to approximately represent one extreme in a spectrum of models for the polar haze. At this extreme, the aggregate particles are relatively large, with mean radius of $\sim$0.7 μm at the 20-mbar level, and have a relatively low column abundance above the 100-mbar level of 4×10^5 cm^{-2}. The opposite extreme is represented by the spherical particle case, for which $D = 3$. At this extreme, the particles are relatively small, with mean radius of $\sim$0.08 μm at the 20-mbar level, and the total column abundance of all particles above the 100-mbar level is 4.4×10^8 cm^{-2}, much higher than for the $D = 2.10$ aggregate case. Since in nature aggregates tend to form with $2 < D < 3$, we expect that mean particle sizes and the column abundance of the polar haze lie somewhere in between these extremes. We also note that our one-dimensional model will tend to overestimate the column abundance of the haze, since any horizontal transport away from the source region will act to spread the particles out over a larger area.

To test the sensitivity of our results to uncertainty in the jovian auroral thermal structure, we also ran the chemical–microphysical model for the cold temperature profile shown in Fig. 2. In general, only a weak dependence of the results on temperature is found. In particular, the properties of the polar haze calculated using the cold profile do not differ significantly from those calculated using the warm profile. The reasons for this behavior can be traced to a general insensitivity of the A_1–A_4 concentrations to temperature profile and to the fact that aerosol nucleation occurs entirely below the 0.1-mbar altitude level in both the warm and cold temperature profile cases. At this altitude and below, the warm and cold profiles are nearly the same (see Fig. 2). The mixing ratio profile of A_1 does not change significantly from that shown in Fig. 3. This relative insensitivity of the A_1 mixing ratio to temperature in the chemical model was previously reported by W00. The peak concentrations of A_2, A_3, and A_4 are found to change by less than a factor of 2 when the colder profile is used. The insensitivity of these concentrations to the temperature profile stems largely from the following three factors: (i) the production rates of A_2, A_3, and A_4 attain their maxima in a layer centered on the 0.1-mbar pressure level, where the cold and warm temperature profiles are essentially the same and equal to the Galileo Atmospheric Structure Instrument nonauroral temperature profile (Seiff *et al.* 1998, Grodent *et al.* 2001); (ii) the concentration of A_1, the parent molecule, is insensitive to the temperature profile; and (iii) the principal loss of A_2, A_3, and A_4 in the model is through photolysis, the rates of which depend only weakly on which temperature profile is used. W00 reported large reductions in the concentrations of A_3 and A_4 in their chemical model when a cold temperature profile was assumed, but these reductions depended on the assumption of efficient condensational removal of these species at relatively low saturation ratios. In the present model, the saturation ratio of A_4 must reach $\sim 10^7$ before significant homogeneous nucleation occurs; the altitude where this saturation ratio occurs for the cold profile is approximately the same as that for the warm profile.

IV. COMPARISON TO OBSERVATIONS

Most of what we know about the physical properties and spatial distribution of the polar haze comes from Pioneer and Voyager spacecraft visible and UV photopolarimetry (Tomasko *et al.* 1978, Hord *et al.* 1979), International Ultraviolet Explorer (IUE) satellite spectrometry (Tomasko *et al.* 1986), Voyager-2 imaging (West 1988), ground-based IR spectrophotometry (Banfield *et al.* 1998), and Galileo Orbiter and Hubble Space Telescope imaging (Rages *et al.* 1999). These data sets primarily constrain the scattering properties, mean size, column abundance, and vertical distribution of the particles.

The most quantitative limits placed on mean particle size come from data analyses by Tomasko *et al.* (1986) and Rages *et al.* (1999). Tomasko *et al.* (1986) analyzed IUE spectra acquired near 40°N latitude. Although centered at midlatitudes, the 3-arcsec aperture of the instrument covered a latitude range of $\sim$9° on the planet. The latitudes covered overlap the latitude range where Vincent *et al.* (2000) found a region of UV-dark haze that remains aligned with the southernmost boundary of the northern auroral oval. Thus there is good reason to believe that the properties of the haze particles determined by the IUE observations represent those of aurorally generated aerosols. This contention is supported by the fact that the mean particle radii determined by Rages *et al.* (1999) for 60°N are very similar to those obtained from the IUE data analysis; however, it should be kept in mind that aerosol column abundances determined from the IUE investigation may be lower than those inside the auroral zone as a consequence of dilution by horizontal atmospheric mixing. Modeling of the limb darkening in the IUE spectra led Tomasko *et al.* (1986) to infer an effective mean particle radius near the $\sim$20-mbar level in the 0.2–0.5 μm range. They argued that particles smaller than $\sim$0.1 μm have a scattering phase function incapable of reproducing the required amount of limb darkening, while particles larger than 0.5 μm would sediment out too rapidly to be sufficiently abundant at high altitudes. However, they did not take into consideration the large fall times associated with fractal aggregates. Our modeling suggests that aggregates with $D = 2.1$ and effective mean radii greater than 0.5 μm can have significant residence times in the jovian stratosphere. Rages *et al.* (1999) analyzed high phase angle Galileo Orbiter images taken in violet and near-IR continuum filters in tandem with Hubble Space Telescope images to determine the vertical distribution and mean particle size of the polar haze at 60°N. Their analysis suggests a mean particle radius of $\sim$0.3 μm near or above the 20-mbar level and $\sim$0.5 μm near or above the 100-mbar level, results which are in accord with the analysis of Tomasko *et al.* (1986).

Our model for fractal aggregates with $D = 2.1$ produces somewhat larger particles than determined by Rages *et al.* for these levels (see Fig. 6b). A model which assumes a higher value of D for the aggregates produces results more in accord with their observations. Figure 7a shows vertical profiles of concentration and Fig. 7b shows the steady-state size distributions

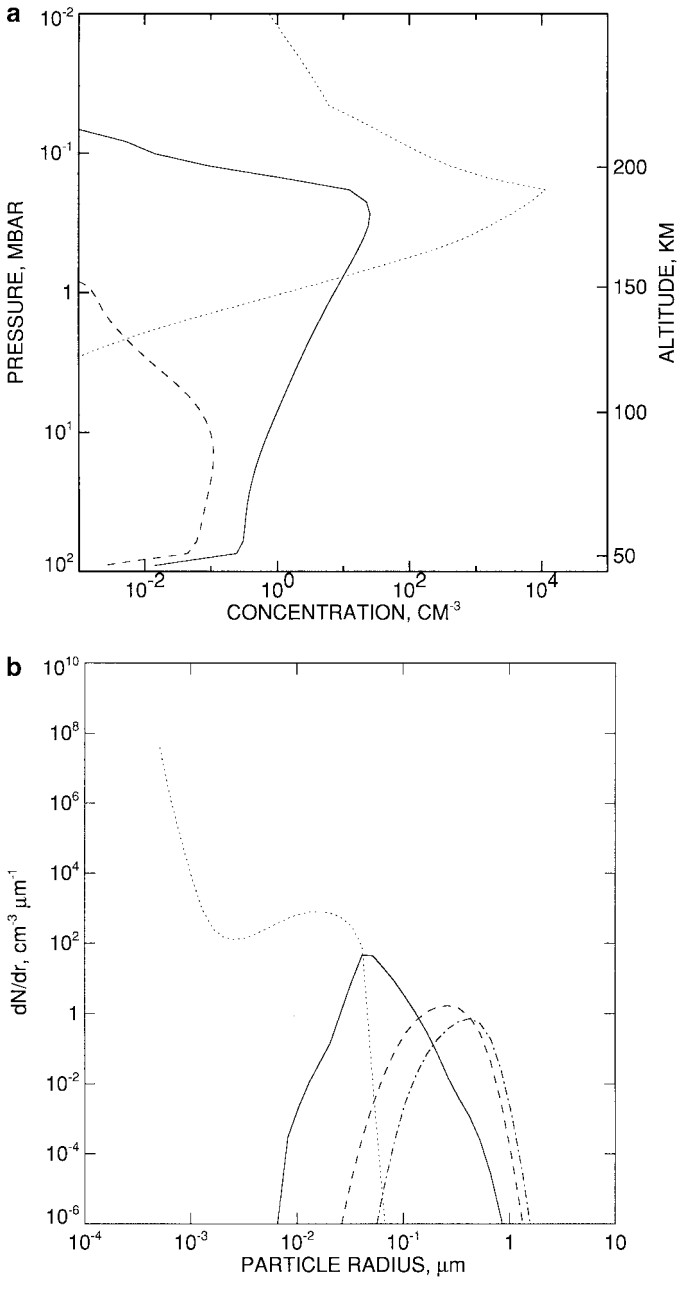

FIG. 7. Results for aggregates with fractal dimension $D = 2.5$. (a) The solid curve is the total concentration of mixed A_2–A_3–A_4 particles with equivalent radii greater than 0.01 μm vs pressure. The dashed curve is the concentration of particles with radii between 0.29 and 0.36 μm. The dotted curve is the total concentration of bare A_3–A_4 nuclei. (b) Size distributions of mixed A_2–A_3–A_4 particles at the 0.5-mbar (solid), 20-mbar (dashed), and 75-mbar (dash-dot) pressure levels. The dotted curve shows the size distribution of bare A_3–A_4 nuclei at the 0.5-mbar level.

for the case $D = 2.5$. For this case, the mean particle radii at the 0.5-mbar, 20-mbar, and 75-mbar pressure levels are 0.05 μm, 0.26 μm, and 0.42 μm, respectively. The computed mean radii at the 20-mbar and 75-mbar levels for $D = 2.5$ are in much better agreement with the data analysis of Rages *et al.* (1999) than the results for $D = 2.1$, and they are also in accord with the range allowed by Tomasko *et al.*'s analysis.

Rages *et al.* also estimated haze number densities for various altitude levels at 60°N. They favored a model in which about 0.13 cm^{-3} of ~0.5-μm particles reside near the 100-mbar level and about 0.7 cm^{-3} of ~0.3-μm particles reside near the 20-mbar level. For comparison, our $D = 2.5$ calculation yields 0.24 cm^{-3} at the 75-mbar level and 0.47 cm^{-3} at the 20-mbar level (see Fig. 7a). However, Rages *et al.* noted that their solution produced too little absorption at 218 nm and too little scattering at 890 nm to be consistent with reflectivities at these wavelengths measured with the Hubble Space Telescope. They found they could provide a much better fit to the IR and UV reflectivities by postulating the presence of a column abundance of $\sim 10^{12}$–$\sim 10^{13}$ cm^{-2} of 0.02-μm particles. West (1988) also inferred that a large abundance of small particles must be present. Our models do produce $\sim 10^{10}$ cm^{-2} of aggregate particles with equivalent radii less than 0.03 μm, but the predicted column abundances fall far short of the value required by Rages *et al.* (1999).

The polar haze is observed to extend in altitude from as deep as the 100-mbar pressure level (Banfield *et al.* 1998, Rages *et al.* 1999) to as high as the ~0.5-mbar level (West 1988). The total concentration profiles shown in Figs. 4, 6, and 7 for the cases $D = 3$, $D = 2.1$, and $D = 2.5$ indicate haze-top levels occurring in the 0.2- to 0.5-mbar pressure range. These haze-top levels can be inferred to be generally consistent with the analysis of West (1988) for 40°N if allowance is made for the fact that our total concentration profiles include a high-altitude component of tiny particles (with radii ~0.01 μm) to which the observations may have been relatively insensitive. Our models do not provide a prediction for the bottom of the polar haze layer, since we assume *a priori* a dynamical removal of particles to the troposphere occurring on a fixed timescale in the 100- to 82-mbar layer.

To fit their IUE data, Tomasko *et al.* (1986) estimated that approximately 5×10^8 cm^{-2} of ~0.2-μm particles was needed to explain the observed absorption optical depth. This estimate implies a total column aerosol loading (expressed in terms of total particle volume per unit area) of 2×10^{-5} cm^3 cm^{-2}. Similarly, the model of Rages *et al.* (1999) that includes a large population of 0.02-μm particles implies a total aerosol loading of $\sim 3 \times 10^{-5}$ cm^3 cm^{-2}. Our models cannot presently account for aerosol loading of this magnitude. For the case of spherical particles ($D = 3$), we calculate a total aerosol loading of 3.7×10^{-7} cm^3 cm^{-2}. The loading increases monotonically with decreasing D, reaching a maximum value of 1.3×10^{-6} cm^3 cm^{-2} when $D = 2.1$. The dependence of total aerosol loading on D in the model stems from the variation of particle residence time with D in the stratosphere, which is illustrated in Fig. 5.

We conclude that, while our models yield haze altitude distributions and mean particle sizes that are consistent with observation, they predict substantially less total aerosol loading than seems to be required by the observations of Tomasko *et al.* (1986), underestimating it by perhaps as much as a factor of 100. One possible explanation is that the current chemical

model may grossly underestimate the mass production rate of condensible material. Pryor and Hord (1991) pointed out that ion and ion–neutral reactions are generally faster than similar reactions involving radical species. Thus ion–molecule reactions not included in the present chemical scheme could conceivably be responsible for producing PAHs at higher rates than predicted, leading to enhancement of nucleation rates and aerosol loading. In addition, the energy flux of precipitating ~30-keV electrons used in the auroral model of Perry *et al.* (1999) and assumed by W00 is nearly a factor of 10 lower than that inferred for the discrete aurorae by Grodent *et al.* (2001). Hence, it is likely that the model of W00 significantly underestimates the total rate of dissociative recombination of CH_5^+ ions, which serves as the primary driving force for the aerosol chemistry in the auroral regions in our model. It must also be noted, however, that the observations themselves are not as yet in complete accord with each other regarding either the total aerosol loading or the size distributions characterizing the polar haze. Systematic errors related to the spatial variability of the polar haze, limited spatial resolution of the IUE observations, and pointing errors could adversely affect the determination of aerosol loading from these data. High-resolution UV and visible images of the polar haze acquired during the Cassini spacecraft's flyby of Jupiter may provide the necessary data to resolve this issue (R. A. West, personal communication). A more precise means of comparing our model results to the observations is also desirable. This would necessarily entail simulating limb intensities and comparing these to observed values.

V. CONCLUSIONS

Understanding the origin, nature, and distribution of the stratospheric haze has direct bearing on questions related to the composition, chemical behavior, and deposition of energy in Saturn's stratosphere and the relation of this deposition of energy to its dynamics. Moreover, stratospheric aerosols that sediment into the troposphere may serve as the condensation nuclei for tropospheric clouds, and thus characterizing their properties may yield valuable information for modeling the formation of the upper-level clouds. Finally, understanding the origin of the high-altitude hazes in the outer planets contributes toward obtaining a better understanding of how nature synthesizes heavy hydrocarbons and other organics and aerosols in space environments.

The results presented here reinforce the initial suggestion by W00 that jovian polar haze formation is a direct result of enhanced production of stable PAHs in Jupiter's auroral regions. This linkage is supported by the geographic correlation between UV-dark haze and maximum auroral precipitation (Pryor and Hord 1991, Vincent *et al.* 2000) and also by the fact that A_2, A_3, and A_4 condense at the right altitudes to be consistent with observational constraints on the vertical distribution of the haze (West 1988, Banfield *et al.* 1998). Moreover, the mean particle radii we predict for the lower stratosphere are generally consistent with the data analyses of Tomasko *et al.* (1986) and Rages *et al.* (1999), particularly if the particles are aggregates with fractal dimension $D \simeq 2.5$.

The calculations demonstrate that the mean particle size and fractal dimension of aggregates should be closely linked. The geometric structure of aggregates affects the way they scatter and polarize light (West 1991). West and Smith (1991) have argued that the scattering and polarizing properties of jovian haze are best explained if the particles are aggregates of small monomers. An important observational goal for the future will be to obtain additional information regarding the geometric structure of the particles through their combined scattering/polarizing properties. This information, combined with determinations of mean particle size, will provide critical data with which to test our understanding of the haze chemistry and microphysics.

The calculations presented here cannot account for the large amount of aerosol loading inferred by Tomakso *et al.* (1986). This suggests that the primarily neutral chemical pathway to heavy hydrocarbon and PAH formation proposed by W00 may proceed too slowly to produce a sufficient amount of condensible species. Pryor and Hord (1991) pointed out that ion and ion–neutral reactions are faster than similar reactions involving radical species. These sorts of reactions may dominate the synthesis of complex hydrocarbons in the auroral zones of the giant planets. Adding ion–molecule reactions to the chemical scheme of W00 could potentially lead to the prediction of higher PAH production rates, higher nucleation rates, and aerosol loading in better agreement with the observations. Clearly, more work needs to be done regarding both neutral–neutral and ion–neutral chemistry in Jupiter's aurorae to obtain a better understanding of the origin and microphysics of jovian polar haze.

New observations that would critically test our models should include a spectral search for low-order, stable PAHs at high altitudes and high latitudes. These species exhibit absorption bands in the near and mid-infrared, particularly in the 3-μm and 12-μm spectral regions (Hudgins and Sanford 1998). The infrared spectra of the cations of these species have also been measured (Hudgins *et al.* 1994). Improved determinations of haze particle shape, size distribution, and total aerosol loading are also critically needed.

ACKNOWLEDGMENTS

We thank R. A. West, K. Rages, M. Lemmon, and S. G. Edgington for helpful discussions. We also thank R. G. Gladstone and an anonymous reviewer for their insightful reviews. Many of the calculations were performed on the Cray SV1 supercomputer managed by the Jet Propulsion Laboratory Supercomputing Project. This work was supported by a grant from the NASA Planetary Atmospheres Program. The work was performed by the Jet Propulsion Laboratory, California Institute of Technology, under contract with the National Aeronautics and Space Administration.

REFERENCES

Banfield, D., B. J. Conrath, P. J. Gierasch, and P. Nicholson 1998. Near-IR spectrophotometry of jovian aerosols: Meridional and vertical distributions. *Icarus* **134**, 11–23.

Chen, C., L. Hung, and H. Hsu 1993. Heterogeneous nucleation of water vapor on particles of SiO_2, Al_2O_3, TiO_2, and carbon black. *J. Colloid Interface Sci.* **157**, 465–477.

Chung, S.-L., Y.-C. Sheu, and M.-S. Tsai 1992. Formation of SiO_2, Al_2O_3, and $3Al_2O_3 \cdot 2SiO_2$ particles in a counterflow diffusion flame. *J. Am. Ceram. Soc.* **75**, 117–123.

Freltoft, T., J. K. Kjems, and S. K. Sinha 1986. Power-law correlations and finite-size effects in silica particle aggregates studied by small-angle neutron-scattering. *Phys. Rev. B* **33**, 269–275.

Frenklach, M., D. W. Clary, W. C. Gardiner, and S. E. Stein 1985. Detailed kinetic modeling of soot formation in shock-tube pyrolysis of acetylene. In *Twentieth Symposium (International) on Combustion*, pp. 887–901. The Combustion Inst., Pittsburgh.

Friedson, A. J. 1998. Formation of refractory grains in Shoemaker-Levy 9 fireballs. *Icarus* **131**, 179–197.

Fuchs, N. A. 1964. *The Mechanics of Aerosols.* Pergamon, New York.

Gladstone, G. R., M. Allen, and Y. L. Yung 1996. Hydrocarbon photochemistry in the upper atmosphere of Jupiter. *Icarus* **119**, 1–52.

Grodent, D., J. H. Waite, and J.-C. Gerard 2001. A self-consistent model of the jovian auroral thermal structure. *J. Geophys. Res.* **106**, 12933–12952.

Hord, C. W., R. A. West, K. E. Simmons, D. L. Coffeen, M. Sato, A. L. Lane, and J. T. Bergstralh 1979. Photometric observations of Jupiter at 2400 Angstroms. *Science* **206**, 956–959.

Hudgins, D. M., and S. A. Sandford 1998. Infrared spectroscopy of matrix isolated polycyclic aromatic hydrocarbons. 1. PAHs containing two to four rings. *J. Phys. Chem. A* **102**, 329–343.

Hudgins, D. M., S. A. Sandford, and L. J. Allamandola 1994. Infrared spectroscopy of polycyclic aromatic hydrocarbon cations. 1. Matrix-isolated naphthalene and perdeuterated naphthalene. *J. Phys. Chem.* **98**, 4243–4253.

Jacobson, M. Z. 1999. *Fundamentals of Atmospheric Modeling*. Cambridge University Press, Cambridge, UK.

Keesee, R. G. 1989. Nucleation and particle formation in the upper atmosphere. *J. Geophys. Res.* **94**, 14683–14692.

Kim, S. J., J. Caldwell, A. R. Rivolo, R. Wagener, and G. S. Orton, 1985. Infrared brightness of Jupiter 3. Spectrometry from the Voyager 1 IRIS experiment. *Icarus* **64**, 233–248.

Kim, S. J., Y. H. Kim, J.-P. Maillard, J. Caldwell, and G. Bjoraker 1995. Four micron continuum of Jupiter. *Icarus* **116**, 423–432.

Lee, A. Y. T., Y. L. Yung, and J. Moses 2000. Photochemical modeling of CH_3 abundances in the outer Solar System. *J. Geophys. Res.—Planets* **105**, 20207–20225.

Meakin, P., and R. Jullien 1988. The effects of restructuring on the geometry of clusters formed by diffusion limited, ballistic, and reaction-limited cluster-cluster aggregation. *J. Chem. Phys.* **89**, 246–250.

Meakin, P., B. Donn, and G. W. Mulholland 1989. Collisions between point masses and fractal aggregates. *Langmuir* **5**, 510–518.

Mountain, R. D., G. W. Mulholland, and H. Baum 1986. Simulation of aerosol agglomeration in the free molecular and continuum flow regimes. *J. Colloid Interface Sci.* **114**, 67–81.

Perry, J. J., Y. H. Kim, J. L. Fox, and H. S. Porter 1999. Chemistry of the jovian auroral ionosphere. *J. Geophys. Res.* **104**, 16541–16565.

Pryor, W. R., and C. W. Hord 1991. A study of Photopolarimeter System UV data on Jupiter, Saturn, Uranus, and Neptune: Implications for auroral haze formation. *Icarus* **91**, 161–172.

Rages, K., R. Beebe, and D. Senske 1999. Jovian stratospheric hazes: The high phase angle view from Galileo. *Icarus* **139**, 211–226.

Richter, H., and J. B. Howard 2000. Formation of polycyclic aromatic hydrocarbons and their growth to soot—A review of chemical reaction pathways. *Progr. Energy Combust. Sci.* **26**, 565–608.

Seiff, A., D. B. Kirk, T. C. D. Knight, R. E. Young, J. D. Mihalov, L. A. Young, F. S. Milos, G. Schubert, R. C. Blanchard, and D. Atkinson 1998. Thermal structure of Jupiter's atmosphere near the edge of a 5-μm hot spot in the north equatorial belt. *J. Geophys. Res.* **103**, 22857–22889.

Smolik, J., and J. Scwartz 1997. Heterogeneous nucleation of naphthalene vapor on water surface. *J. Colloid Interface Sci.* **185**, 382–389.

Smolik, J., and V. Zdimal 1993. Homogeneous nucleation of supersaturated vapors. A comparison of experimental results with theory. *Coll. Czech. Chem. Commun.* **58**, 2831–2835.

Smolik, J., J. Vitovek, and J. Vasakova 1986. Nucleation in supersaturated vapors of solid and liquid naphthalene and phthalic anhydride. *Coll. Czech. Chem. Commun.* **51**, 1551–1561.

Strobel, D. 1983. Photochemistry of the reducing atmospheres of Jupiter, Saturn, and Titan. *Int. Rev. Phys. Chem.* **3**, 145–176.

Tomasko, M. G., R. A. West, and N. D. Castillo 1978. Photometry and polarimetry of Jupiter at large phase angles. I. Analysis of imaging data of a prominent belt and a zone from Pioneer 10. *Icarus* **33**, 558–592.

Tomasko, M. G., E. Karkoschka, and S. Martinek 1986. Observations of the limb darkening of Jupiter at ultraviolet wavelengths and constraints on the properties and distribution of stratospheric aerosols. *Icarus* **65**, 218–243.

Toon, O. B., R. P. Turco, D. Westphal, A. Malone, and M. S. Liu. 1988. A multidimensional model for aerosols: Description of computational analogs. *J. Atmos. Sci.* **45**, 2123–2143.

Trafton, L. M., J. C. Gerard, G. Munhoven, and J. H. Waite, Jr. 1994. High-resolution spectra of Jupiter's northern auroral ultraviolet emission with the Hubble Space Telescope. *Astrophys. J.* **421**, 816–827.

Turco, R. P., O. B. Toon, R. C. Whitten, R. G. Keesee, and D. Hollenbach 1982. Noctilucent clouds: Simulation studies of their genesis, properties and global influences. *Planet. Space Sci.* **30**, 1147–1181.

Ulrich, G. D. 1971. Theory of particle formation and growth in oxide synthesis flames. *Combust. Sci. Technol.* **4**, 47–57.

Vincent, M. B., J. T. Clarke, G. E. Ballester, W. M. Harris, R. A. West, J. T. Trauger, R. W. Evans, K. R. Stapelfeldt, D. Crisp, C. J. Burrows, J. S. Gallagher III, R. E. Griffiths, J. J. Hester, J. G. Hoessel, J. A. Holtzman, J. R. Mould, P. A. Scowen, A. M. Watson, and J. A. Westphal 2000. Jupiter's polar regions in the ultraviolet as imaged by HST/WFPC2: Auroral-aligned features and zonal motions. *Icarus* **143**, 205–222.

Wang, H., and M. Frenklach 1994. Calculations of rate coefficients for the chemically activated reactions of acetylene with vinylic and aromatic radicals. *J. Phys. Chem.* **98**, 11465–11489.

West, R. A. 1988. Voyager 2 imaging eclipse observations of the jovian high altitude haze. *Icarus* **75**, 381–398.

West, R. A. 1991. Optical properties of aggregate particles whose outer diameter is comparable to the wavelength. *Appl. Opt.* **30**, 5316–5324.

West, R. A., A. J. Friedson, and J. F. Appleby 1992. Jovian large-scale stratospheric circulation. *Icarus* **100**, 245–259.

West, R. A., and P. H. Smith 1991. Evidence for aggregate particles in the atmospheres of Titan and Jupiter. *Icarus* **90**, 330–333.

Wong, A.-S., A. Lee, Y. L. Yung, and J. M. Ajello 2000. Jupiter: Aerosol chemistry in the polar atmosphere. *Astrophys. J.* **534**, L215–217.

Zachariah, M. R., and H. G. Semerjian 1989. Simulation of ceramic particle formation: Comparison with in-situ measurements. *AIChE J.* **35**, 2003–2012.